Nature Communications

https://doi.org/10.1038/s41467-026-73082-4

Article in Press

Unconventional density-wave state in Ruddlesden–Popper nickelate $La_4Ni_3O_{10}$

Received: 12 April 2025

Accepted: 29 April 2026

Cite this article as: Wang, Y., Zhao, D., Zhang, E. *et al.* Unconventional density-wave state in Ruddlesden–Popper nickelate $La_4Ni_3O_{10}$. *Nat Commun* (2026). https://doi.org/10.1038/s41467-026-73082-4

Yu Wang, Dan Zhao, Enkang Zhang, Lixing Chen, Yanbing Zhou, Mengzhu Shi, Yinghao Zhu, Jianjun Ying, Jun Zhao & Tao Wu

Unconventional density-wave state in Ruddlesden–Popper nickelate $La_4Ni_3O_{10}$

Yu Wang[1‡], Dan Zhao[1‡], Enkang Zhang[2‡], Lixing Chen[2], Yanbing Zhou[1], Mengzhu Shi[1], Yinghao Zhu[2], Jianjun Ying[3,5], Jun Zhao[2,5,*], Tao Wu[1,3,4,5,*]

1. Hefei National Research Center for Physical Sciences at the Microscale, University of Science and Technology of China, Hefei 230026, China
2. State Key Laboratory of Surface Physics and Department of Physics, Fudan University, Shanghai 200433, China
3. CAS Key Laboratory of Strongly Coupled Quantum Matter Physics, Department of Physics, University of Science and Technology of China, Hefei 230026, China
4. Collaborative Innovation Center of Advanced Microstructures, Nanjing University, Nanjing 210093, China
5. Hefei National Laboratory, University of Science and Technology of China, Hefei 230088, China

‡These authors contributed equally to this work
*Correspondence to: zhaoj@fudan.edu.cn, wutao@ustc.edu.cn

Abstract:

The recent discovery of superconductivity in Ruddlesden–Popper (RP) nickelates $R_{n+1}Ni_nO_{3n+1}$ (R = rare earth) under high pressure provides a new platform to understand the underlying physics of high-temperature superconductivity. Previous transport measurements suggest a notable correlation between pressure-induced high-temperature superconductivity and a density-wave (DW) state. Therefore, identifying the nature of the DW state is a prerequisite for decoding the superconducting mechanism in the new family of high-temperature superconductors. Here, we report a comprehensive investigation of the ambient-pressure DW transition in high-quality $La_4Ni_3O_{10}$ single crystals using ^{139}La (I = 7/2) nuclear magnetic resonance (NMR) and nuclear quadrupole resonance (NQR). Our findings reveal a two-stage evolution of the DW order. Below $T^* \approx 150$ K, a short-range charge order develops in the inner Ni-O layer, accompanied by a dramatic enhancement of spin fluctuations. This is followed by a DW transition at T_{DW}

≈ 133 K, establishing fully developed charge and spin orders across all Ni-O planes. The layer-dependent behaviour highlights that the mechanism of DW transitions in $La_4Ni_3O_{10}$ may involve both the interlayer coupling and the electronic structure disparities between the inner and outer layers. These findings provide a new framework for understanding the complex DW state in RP nickelates and their potential role in high-temperature superconductivity.

Introduction

A hallmark of the phase diagram in high-T_c superconductors is the presence of multiple electronic orders. These electronic orders not only compete but also exhibit complex interweaving, making their interplay crucial for understanding the emergence of superconductivity [1,2]. The recent discovery of pressure-induced superconductivity in double- and trilayer Ruddlesden−Popper (RP) nickelates $R_{n+1}Ni_nO_{3n+1}$ (R = rare earth) provides a new platform for investigating the role of intertwined electronic orders [3–8]. To date, two density-wave (DW) transitions have been experimentally identified in the bilayer nickelate $La_3Ni_2O_7$ at ambient pressure [9,10]. One is a spin-density-wave (SDW) transition at ~150 K, which has been confirmed by various experimental techniques, including resonant X-ray scattering (RIXS), neutron scattering, nuclear magnetic/quadrupole resonance (NMR/NQR) and muon spin rotation (μSR) [11–17]. The other, inferred from transport and optical conductivity experiments, corresponds to a charge-density-wave (CDW) transition occurring between 110 K and 140 K [9,18–20]. Interestingly, these two DW transitions exhibit opposite pressure-dependent evolutions in $La_3Ni_2O_7$ [13,16]. These findings indicate that the exact nature of the DW ordering in $La_3Ni_2O_7$ remains a subject of ongoing debate.

Similar to $La_3Ni_2O_7$, the trilayer RP nickelate $La_4Ni_3O_{10}$ also hosts a DW transition at ambient pressure [6–8,21–26]. Under high pressure, the DW transition is progressively suppressed, eventually giving way to the emergence of superconductivity [6–8,23,24]. Previous studies have indicated that the CDW and SDW transitions occur simultaneously at ambient pressure, with a transition temperature (T_{DW}) of ~135 K [21]. Moreover, the DW state displays an intriguing layer dependence, where the spin modulation exhibits a node in the inner Ni-O plane, whereas an in-phase CDW order exists throughout the trilayer Ni-O block [21]. Experimentally, the direct detection of such a layer-dependent DW state within individual Ni-O layers remains challenging. Structurally, the trilayer system contains two inequivalent crystalline positions for the ^{139}La nuclei, designated as La(1) and La(2) in Fig. 1(a). This feature provides a unique opportunity to employ site-selective NMR and NQR measurements to clarify the nature of the DW order in each Ni-O layer. In the present work, we performed ^{139}La NMR/NQR studies on a high-quality $La_4Ni_3O_{10}$ single crystal. Our results reveal an unusual layer-dependent CDW state, which sheds new light on the nature of the DW state in RP nickelate superconductors.

Results

NMR spectra and site assignments

As shown in Fig. 1(a), $La_4Ni_3O_{10}$ crystallizes in a layered monoclinic structure (crystal space group *P2₁/a*) at ambient pressure [6–8,27,28]. The corner-sharing NiO_6 octahedra form trilayer Ni-O planes that stack along the *c*-axis and are separated by La-O fluorite-type layers. Structurally, two inequivalent La sites exist in the trilayer RP structure. The La sites located within the Ni-O octahedra are designated as La(1), whereas those in the La-O fluorite-type layers are defined as La(2). Given their distinct local environments, the La(2) site is influenced primarily by the electronic states of the outer Ni-O planes, whereas the La(1) site probes the electronic features of both the inner and outer Ni-O planes.

Owing to the monoclinic symmetry, the crystal axis *c* is tilted relative to the vertical axis. We define the *c**-axis as the direction perpendicular to the *ab*-plane for convenience. Figure 1(b) displays the standard full NMR spectra with external magnetic field **B**//*c**, measured both above and below the DW transition. Because ^{139}La has a spin number of I = 7/2, each site exhibits seven NMR transition lines: one central transition line and six satellites arising from quadrupole interactions. By utilizing their distinct quadrupole frequencies and Knight shifts [4,29–31], we can distinguish the La(1) and La(2) sites in the NMR spectra (labelled in Fig. 1(b)), thereby enabling site-selective measurements.

Based on the satellite frequencies and angle-dependent measurements (Supplementary Note 1), we conclude that the principal axes of the electric field gradient (EFG) at both La sites deviate from the *c**-axis. Consequently, when **B**//*c**, quadrupole interactions perturb the central transition lines. In the second-order approximation, the central transition frequency is expressed as:

$$f_c = (1 + K_0)\gamma B + \frac{v(m, v_q, \eta, \theta, \varphi)}{(1+K_0)\gamma B}. \qquad (1)$$

Here, K_0 is the Knight shift and $\nu(m,\nu_q,\eta,\theta,\varphi)$ originates from quadrupole interactions; θ and φ are the polar and azimuthal angles of **B** relative to the EFG principal axis. Given the orthorhombic twins within the *ab*-planes and the orientations of the principal axis, the slight deviation of **B** from the *c**-axis introduces variations in the second-order terms, thereby generating additional spectral splitting in Fig. 1(b) (Supplementary Note 2). To minimize these influences, we employed a dual-axis goniometer probe, carefully adjusting the sample orientation to align **B** precisely along the *c**-axis (Supplementary Note 2).

Furthermore, NQR serves as a sensitive probe of the local environment. Previous studies have reported that the quadrupole frequency of the La(1) site (~2.2 MHz) is lower than that of the La(2) site (~5.2 MHz) in $La_4Ni_3O_{10}$, which makes the measurement of La(1)-NQR particularly challenging [4,29–31]. Owing to the broadened linewidth and weak NQR signal intensity at the La(1) site (Supplementary Note 3), we specifically targeted its ±5/2 ↔ ±7/2 transition. The full NQR spectra were also acquired for the La(2) site. As shown in Fig. 1(c) and (e), both the La(1) and La(2) spectra display a single-peak structure in the paramagnetic state, confirming a unique local environment for each site. Moreover, frequency-sweep measurements spanning 13.5 MHz to 19 MHz reveal no additional resonance peaks other than the ±5/2 ↔ ±7/2 transition for the La(2) site in Fig. 1(d), further ruling out the presence of impurity phases [4]. Collectively, these results confirm the single-phase nature and high quality of our single crystals.

Evidence for a SDW transition

Next, we measured the temperature-dependent NMR spectra and nuclear spin-lattice relaxation rates ($1/T_1$) at both the La(1) and La(2) sites with **B**//*c**. Figure 2(a) displays central transition lines of the La(1) site. Upon cooling, the NMR spectra begin to broaden symmetrically at ~150 K, eventually developing a double-peak-like structure below ~133 K. To quantitatively analyse the evolution of the central transition lines, we extracted the temperature-dependent full width at half maximum (FWHM). As shown in Fig. 2(d), the FWHM rapidly increases beginning at ~150 K and then gradually saturates below ~133 K. In principle, either CDW or SDW could induce the observed broadening. Here, we confirm that these spectral features are predominantly driven by the SDW order.

As shown in Fig. 2(b), the double-peak-like lineshape at ~2.2 K is almost field-independent from 9 T to 15.5 T. Generally, the linewidth below the DW transition temperature can be expressed as:

$$\Delta f = \sqrt{\Delta f_{para}^2 + \Delta f_q^2 + \Delta f_{mag}^2} \quad . \qquad (2)$$

Here, $\Delta f_{para} \propto \Delta KB$ represents the Knight-shift inhomogeneity, $\Delta f_q \propto 1/B$ arises from the quadrupole effect and $\Delta f_{mag} \propto \gamma|B_{int}|$ (where $B_{int} << B$) originates from the internal magnetic field (B_{int}) generated by the spin order. The charge order can broaden the NMR spectra through both the quadrupole effect (Δf_q) and the Knight-shift inhomogeneity (Δf_{para}) [32]. These contributions typically result in a field-dependent effect. Therefore, the field-independent lineshape is caused mainly by the SDW order. Moreover, guided by previous neutron scattering studies that suggest an incommensurate spin modulation with a wave vector $\mathbf{q}_s$ = (0, 0.62) [21], we simulated the NMR spectral lineshape in Fig. 2(c). This result revealed that the incommensurate magnetic structure naturally leads to a double-peak-like feature, which further clarifies the magnetic origin of the broadening (Supplementary Note 4). These observations strongly indicate the formation of a long-range SDW order below $T \approx 133$ K, which is consistent with previous results [21,24].

The SDW transition is also evidenced by the nuclear spin-lattice relaxation rate ($1/T_1$). Typically, $1/T_1$ is related to the imaginary part of the magnetic susceptibility ($\chi''_\perp(q,\omega_n)$), which is defined as: $\frac{1}{T_1} = 2\gamma^2 T \sum_q A_\perp^2(q) \frac{\chi''_\perp(q,\omega_n)}{\omega_n}$. During an antiferromagnetic phase transition, $\chi''_\perp(q,\omega_n)$ diverges at the antiferromagnetic wave vector as the temperature approaches the transition temperature, thereby resulting in a pronounced increase in $1/T_1T$. As shown in Fig. 2(e)–(f), the $1/T_1T$ at both the La(1) and La(2) sites exhibit critical spin fluctuations upon approaching $T \approx 133$ K, indicating a SDW transition (Supplementary Note 5). This finding aligns with the formation temperature of the double-peak-like lineshape observed in the NMR spectra in Fig. 2(a). Below ~133 K, $1/T_1T$ sharply decreases, but its magnitude exhibits only a relatively weak change across this transition. This behaviour is distinct from that in polycrystalline $La_4Ni_3O_{10}$, where a clear signature of gap opening is observed in $1/T_1T$ [29–31]. This discrepancy likely originates from stronger spin fluctuations in the single crystal, obscuring the details of the density of states (Supplementary Note 5).

Additionally, in the temperature range of 133 K < T < 150 K, the spin dynamics may become more sensitive to disorder effects, thereby promoting the development of short-range spin order. Consequently, this short-range spin order broadens the La(1) central transition line above $T \approx 133$ K. In this scenario, the lineshape can be further interpreted as the coexistence of two components: a paramagnetic-state-like component, highlighted by the dashed rectangle in Fig. 2(a), and a broadening component on both sides, influenced by short-range spin order.

Upon further cooling, an additional decrease in $1/T_1T$ is also observed below ~25 K, while the NMR spectra in Fig. 2(a) remain essentially unchanged. This indicates a possible dynamic crossover behaviour. Furthermore, field-dependent $1/T_1T$ indeed shows possible spin freezing below ~25 K (Supplementary Note 6). This behaviour has also been observed in $La_3Ni_2O_7$ [13] and slightly doped La_2CuO_4 [33] below the SDW transition. However, this is not the focus of the present study.

Evidence for short-range charge order in the inner Ni-O layer above T_{DW}

In addition to the SDW order, a CDW order has been identified in $La_4Ni_3O_{10}$ by X-ray diffraction (XRD) and scanning tunneling microscopy (STM) at ambient pressure [21,26]. The central transition lines are primarily responsive to the spin order. In contrast, the NMR satellites and the NQR spectra are highly sensitive to changes in the EFG, rendering them effective tools for probing charge ordering [34,35]. The frequencies of the first satellites and NQR lines are described by the following expressions, respectively:

$$f_{\text{sate}} = f_c \pm 0.5\nu_q\,(3\cos^2\theta - 1 + \eta\,\sin^2\theta\,\cos2\varphi) \quad (3) \quad \text{and}$$

$$f_q = \nu_q/6\,[3I_z^2 - I^2 + \eta\,(I_x^2 - I_y^2)] \; (4).$$

Here, f_c represents the frequency of the central transition line, ν_q is the quadrupole frequency and η is the asymmetry parameter. In the following, we further investigate these NMR satellites and NQR spectra to explore the CDW order in $La_4Ni_3O_{10}$.

The temperature dependences of the first low- and high-frequency NMR satellites (hereafter called LF1 and HF1, respectively) for both the La(1) and La(2) sites are summarized in Fig. 3(a)-(b). In the paramagnetic state, these satellites display sharp and symmetrical single-peak lineshapes.

We first focus on the results from the La(1) satellites. In Fig. 3(a), the dashed lines track the temperature evolution of the LF1 and HF1 peak frequencies. To quantify the changes, we extracted the corresponding frequency difference (Δf) between the peak maxima, as summarized in Fig. 3(c). Upon cooling, Δf exhibits a clear anomaly below $T^* \approx 150$ K, deviating from its behaviour in the paramagnetic state. This anomalous frequency shift typically reflects changes in the EFG. Generally, the charge anomaly can alter the EFG of the nuclei, modifying not only the magnitudes of v_q and η, but also the orientation of the EFG principal axes. Both effects contribute to Δf. Consequently, the anomalous shift in Δf below T^* serves as a quantitative indicator of a charge anomaly, although it remains ambiguous which of these contributions dominates the observed changes. Furthermore, as shown in Fig. 3(e), both LF1 and HF1 broaden below ~150 K and develop asymmetric lineshapes, with their spectral weights shifting toward larger v_q. The asymmetrical lineshapes of the LF1 and HF1 satellites exhibit approximate mirror symmetry about the central transition frequency. This typically arises from the sign reversal of the EFG contribution between these two satellites. At the same temperature, the central transition lines maintain a symmetrical lineshape in Fig. 2(a) (Supplementary Fig. 7). This distinct difference in lineshapes between the satellites and central transition lines suggests that the mechanisms for their respective broadening differ. Therefore, changes in La(1)-EFG can be inferred from the satellite lineshapes below T^*. These observations collectively provide clear evidence for a charge anomaly occurring at $T^* \approx 150$ K.

A previous report indicated that the CDW order existed in all the Ni-O planes [21]. If this was the case, then the La(2) site should also exhibit a similar response to the charge anomaly. However, above ~133 K, both LF1 and HF1 of the La(2) site retain a symmetric lineshape, and Δf evolves smoothly with decreasing temperature. For comparison, representative spectra measured at $T = 142$ K are shown in Fig. 3(g). At this temperature, the La(1) satellites already exhibit a clearly asymmetric shape, whereas those of the La(2) site remain symmetric. This stark contrast confirms the absence of significant EFG changes at the La(2) site above ~133 K.

Furthermore, distinct changes in EFG were detected via ^{139}La-NQR measurements. Owing to the broadened linewidth and weak signal intensity of La(1)-NQR, we focused on measuring the La(1)-3v_q quadrupole resonance lines in Fig. 4(a). We obtained the values of v_q and η by analysing the frequencies of its NMR satellites in Fig. 3(c) and the NQR-3v_q lines in Fig. 4(a), under the assumption that the direction of its EFG principal axis remains fixed (Supplementary Note 8). The results are displayed in Fig. 4(c) and (e). Below $T^* \approx 150$ K, both v_q and η exhibit a pronounced deviation from their high-temperature trends. In contrast, for the La(2) site, both v_q and η in Fig. 4(d)-(f), extracted from the 2v_q and 3v_q frequencies, exhibit smooth evolution across 150 K upon cooling (Supplementary Note 9).

Considering that the La(2) site primarily couples to the outer Ni-O planes shown in Fig. 1(a), the absence of a noticeable response at this site below ~150 K suggests that the charge anomaly does not develop immediately in the outer Ni-O planes. However, the La(1) site can couple to both the inner and outer Ni-O layers. The charge anomaly at ~150 K occurs exclusively in the inner Ni-O layer, which naturally explains the absence of a charge-related response at the La(2) site.

To further understand the charge anomaly observed near 150 K, we performed specific heat measurements (Supplementary Fig. 10). We did not observe a pronounced specific heat anomaly around 150 K. In contrast, as a local microscopic probe, NMR clearly detected a change in the La(1) EFG below 150 K as discussed above. These results suggest that the charge anomaly below 150 K likely originates from short-range charge order rather than long-range charge order. Usually, the gradual freezing of charge fluctuations offers a natural explanation for this short-range charge order above the DW transition temperature. However, the observed short-range charge order forms exclusively in the inner Ni-O layer, which is distinct from the long-range charge order below the DW transition temperature (see Fig. 5) [21]. One appealing scenario for such a short-range charge order is related to a quasi-two-dimensional CDW order occurring in the inner Ni-O layer. In the two-dimensional limit, the proliferation of topological defects could destroy the long-range order, which leads to a topological phase transition (Berezinskii–Kosterlitz–Thouless transition) instead of a conventional Landau phase transition[36–38]. Previous calculations indicate that the Berezinskii–Kosterlitz–Thouless transition suppresses the signature of phase transition in specific heat and only leads to a broad crossover behaviour [39]. Therefore, the phase transition to a quasi-two-dimensional CDW order might be invisible in the specific heat. This interesting possibility requires further investigation in future research.

The formation of the short-range charge order also reflects significant interplay with the spin degrees of freedom. As shown in Fig. 2(e)–(f), $1/T_1T$ increases immediately below ~150 K, suggesting enhanced spin fluctuations (Supplementary Note 5). The stretched exponent r ($0 < r \leq 1$), which represents the inhomogeneity of spin dynamics [40], also rapidly decreases below ~150 K in Fig. 2(g). These behaviours of spin dynamics are similar to those observed in striped cuprate superconductors, where spin fluctuations are also significantly enhanced just below the charge ordering temperature [41–45]. Moreover, in $La_4Ni_3O_{10}$, the enhanced spin fluctuations can also extend to the outer Ni-O plane without a charge anomaly, which leads to a collective increase in $1/T_1T$ across the trilayer block, as observed at both the La(1) and La(2) sites. This feature may imply the presence of pivotal interlayer interactions, which has also been discussed in recent theoretical studies [46–50].

Evidence for an outer-layer charge order below T_{DW}

Having discussed the charge anomaly within the 133 K–150 K range, we now turn to the analysis of its properties below $T_{DW} \approx 133$ K. As shown in Fig. 3(b), upon further cooling, the La(2) satellites undergo abrupt broadening and develop a pronounced asymmetry below ~133 K. To quantify this behaviour, the temperature-dependent FWHM for both the LF1 and HF1 satellites is summarized in Fig. 3(f). The FWHM initially increases gradually below $T \approx 150$ K, which can be attributed to the emergence of short-range spin order. This is followed by a sharp increase at $T \approx 133$ K. Owing to the larger hyperfine field at the La(2) site [31], the spectral linewidth is dominated by magnetic contributions below $T \approx 133$ K. However, it is noteworthy that the FWHM and lineshapes of the LF1 and HF1 satellites differ significantly, with LF1 exhibiting a substantially broader linewidth than HF1 does. Given that the magnetic broadening is expected to be equivalent for low- and high-frequency satellites, the observed differences in linewidth and lineshape cannot be attributed solely to magnetic origins. This implies that an additional EFG modulation on the La(2) satellites must be considered. Analogous spectral features have also been reported in cuprates [32,34,51,52], which may suggest an intricate coupling between the modulated magnetism, the Knight shift and the EFG contribution to the satellites in the spin and charge ordering states. Taken together, these features collectively suggest the emergence of a CDW order in the outer layer below $T \approx 133$ K.

Discussion

Concerning spin order, the temperature-dependent spectra and $1/T_1T$ confirm a SDW transition at $T \approx 133$ K. However, the current ^{139}La NMR data cannot be used to determine the layer dependence. Structurally, the La(1) site couples to both the inner and outer Ni-O planes, whereas the La(2) site is primarily influenced by the electronic states of the outer Ni-O planes. As long as the SDW exists in the outer layers, both the La(1) and La(2) sites are expected to detect its presence. Consequently, our ^{139}La NMR experiments cannot definitively determine whether the inner layer is nonmagnetic. Previous neutron scattering data indicated an absence of magnetic order in the inner layer [21]. Recent μSR experiments suggest the possible existence of tiny magnetic moments therein [24]. Theoretically, the inner layer is also predicted to possess nearly zero magnetic moment, close to a nonmagnetic state [53,54].

By integrating the site-selective ^{139}La-NMR/NQR results with the current understanding of SDW order[24,53,54], we propose a comprehensive scenario for the temperature-dependent evolution of DW states in $La_4Ni_3O_{10}$, as summarized in Fig. 5. For charge degrees of freedom, a short-range charge order initially emerges in the inner Ni-O layer below $T^* \approx 150$ K. Upon further cooling, a long-range CDW order develops across the trilayer Ni-O plane at $T_{DW} \approx 133$ K. The spin degrees of freedom undergo a similar evolution from short-range correlations to long-range order, although our ^{139}La-NMR measurements cannot fully resolve layer-dependent features. At present, the neutron scattering data indicate a nonmagnetic inner layer [21], whereas recent μSR experiments point to the possible existence of tiny magnetic moments [24].

Previous XRD and neutron scattering studies have revealed simultaneous SDW and CDW transitions in $La_4Ni_3O_{10}$, characterized by correlated wave vectors satisfying $\mathbf{q}_{\mathbf{CDW}} = 2\mathbf{q}_{\mathbf{SDW}}$ [21]. Further evidence from angle-resolved photoemission spectroscopy (ARPES) [55], optical spectroscopy [22,56], and STM [26] consistently reveals that the opening of an energy gap coincides with DW formation. These collective observations also suggest a potential Fermi-surface nesting scenario. Furthermore, random-phase-approximation (RPA) calculations predict that the nesting vector $\mathbf{q} \sim (\pm 0.7\pi, 0)$ between the two Fermi pockets originating from the outer Ni-O planes is very close to the experimental value [54]. While the nesting scenario plausibly accounts for the formation of the SDW, the origin of the CDW remains unclear. Our findings provide important insights into the underlying microscopic mechanisms. First, the temperature-dependent $1/T_1T$ exhibits a strong enhancement, which coincides with the onset of the short-range charge order shown in Fig. 2(e)-(f). This behaviour is strikingly similar to that observed in striped cuprates [41–45]. This suggests a significant interplay between the spin and charge degrees of freedom, implying a possible magnetic driving mechanism [57]. Second, the present work demonstrates that the CDW modulations in $La_4Ni_3O_{10}$ display unique layer-dependent characteristics: The charge degrees of freedom initiate as short-range correlations in the inner Ni-O plane and eventually form a trilayer CDW order. This layer-dependent feature suggests that the mechanism of DW transitions in $La_4Ni_3O_{10}$ may involve both the interlayer coupling and the electronic structure disparities between the inner and outer layers. Theoretical calculations indeed indicate that the electron correlation effects in the outer layer are stronger than those in the inner Ni-O plane and underscore the critical role of interlayer coupling [46–50,54,58–61].

Recently, a spin-spinless magnetic structure has been proposed for $La_3Ni_2O_7$ [31]. In $La_4Ni_3O_{10}$, the SDW state in the trilayer structure also exhibits a similar spin-spinless pattern (↑, 0, ↓), with the inner layer being nearly nonmagnetic and the outer layers being spin-polarized. These analogous features suggest that the two systems may share underlying physical mechanisms. In the bilayer system $La_3Ni_2O_7$, interlayer antiferromagnetic exchange interactions are considered crucial for the emergence of superconductivity [11,62]. However, in $La_4Ni_3O_{10}$, the trilayer structure may introduce a more complicated interlayer coupling [47,50], which might partially account for the lower superconducting transition temperature under pressure compared to $La_3Ni_2O_7$.

Methods

Growth and characterization of single crystals

High-quality $La_4Ni_3O_{10}$ single crystals were synthesized using an optical floating-zone technique. During the crystal growth process, the oxygen pressure was maintained at 18 – 22 bar [7]. A single crystal with dimensions of approximately 1 × 1 × 1 mm^3 was selected for the NMR experiments. For the NQR experiments, multiple crystals selected from the same growth batch were used. The phase purity of all samples was verified via broad frequency-sweep NQR measurements spanning 13.5 to 19 MHz (Fig. 1(d)), which definitively ruled out the presence of impurity phases. The DW transition was confirmed via temperature-dependent specific heat measurements, performed using a Physical Property Measurement System (PPMS-9 T, Quantum Design).

NMR and NQR measurements

A commercial NMR spectrometer from Thamway Co. Ltd. was used for the NMR and NQR measurements. An NMR-quality magnet from Oxford Instruments offered a uniform magnetic field up to 15.5 T. The samples were compactly packed into copper coils. The precise external magnetic field at the sample position was calibrated using the ^{63}Cu NMR resonance of the coil itself. All the NMR and NQR spectra were measured via the standard spin-echo method with a fast Fourier transform sum.

The nuclear spin-lattice relaxation time (T_1) of the central transition line ($I = 7/2$) was measured using the standard saturation recovery method. The time-dependent recovery of the nuclear magnetization $M(t)$ was fitted by the following function:

$$1-\frac{M(t)}{M(\infty)}=\frac{1}{84}exp\left(-\left(\frac{t}{T_1}\right)^r\right)+\frac{3}{44}exp\left(-\left(\frac{6t}{T_1}\right)^r\right)+\frac{75}{364}exp\left(-\left(\frac{15t}{T_1}\right)^r\right)+\frac{1225}{1716}exp\left(-\left(\frac{28t}{T_1}\right)^r\right).$$

Here, r is the stretched exponent ($0 < r \leq 1$). Typical recovery curves are shown in Supplementary Fig. 11.

Data availability

The data generated in this study have been deposited in the figshare database under accession code https://doi.org/10.6084/m9.figshare.31449508.

Code availability

The codes that support the findings of this study are available from the corresponding author.

Reference

1. Fradkin, E., Kivelson, S. A. & Tranquada, J. M. Colloquium: Theory of intertwined orders in high temperature superconductors. *Rev. Mod. Phys.* **87**, 457–482 (2015).

2. Fernandes, R. M., Orth, P. P. & Schmalian, J. Intertwined vestigial order in quantum materials: Nematicity and beyond. *Annu. Rev. Condens. Matter Phys.* **10**, 133–154 (2019).

3. Sun, H. *et al.* Signatures of superconductivity near 80 K in a nickelate under high pressure. *Nature* **621**, 493–498 (2023).

4. Wang, N. *et al.* Bulk high-temperature superconductivity in pressurized tetragonal $La_2PrNi_2O_7$. *Nature* **643**, 579–584 (2024).

5. Sakakibara, H. *et al.* Theoretical analysis on the possibility of superconductivity in the trilayer Ruddlesden-Popper nickelate $La_4Ni_3O_{10}$ under pressure and its experimental examination: Comparison with $La_3Ni_2O_7$. *Phys. Rev. B* **109**, 144511 (2024).

6. Li, Q. *et al.* Signature of Superconductivity in Pressurized $La_4Ni_3O_{10}$. *Chin. Phys. Lett.* **41**, 017401 (2024).

7. Zhu, Y. *et al.* Superconductivity in pressurized trilayer $La_4Ni_3O_{10-\delta}$ single crystals. *Nature* **631**, 531–536 (2024).

8. Zhang, M. *et al.* Superconductivity in trilayer nickelate $La_4Ni_3O_{10}$ under pressure. *Phys. Rev. X* **15**, 021005 (2025).

9. Liu, Z. *et al.* Evidence for charge and spin density waves in single crystals of $La_3Ni_2O_7$ and $La_3Ni_2O_6$. *Sci. China Phys. Mech. Astron.* **66**, 217411 (2023).

10. Wang, M., Wen, H.-H., Wu, T., Yao, D.-X. & Xiang, T. Normal and superconducting properties of $La_3Ni_2O_7$. *Chin. Phys. Lett.* **41**, 077402 (2024).

11. Chen, X. *et al.* Electronic and magnetic excitations in $La_3Ni_2O_7$. *Nat. Commun.* **15**, 9597 (2024).

12. Plokhikh, I. *et al.* Unraveling Spin Density Wave Order in Layered Nickelates $La_3Ni_2O_7$ and $La_2PrNi_2O_7$ via Neutron Diffraction. *arXiv:2503.05287* (2025).

13. Zhao, D. *et al.* Pressure-enhanced spin-density-wave transition in double-layer nickelate $La_3Ni_2O_{7-\delta}$. *Sci. Bull.* **70**, 1239–1245 (2025).

14. Yashima, M. *et al.* Microscopic Evidence for Spin–Spinless Stripe Order with Reduced Ni Moments within ab Plane for Bilayer Nickelate $La_3Ni_2O_7$ Probed by ^{139}La-NQR. *J. Phys. Soc. Jpn.* **94**, 054704 (2025).

15. Chen, K. *et al.* Evidence of Spin Density Waves in $La_3Ni_2O_{7-\delta}$. *Phys. Rev. Lett.* **132**, 256503 (2024).

16. Khasanov, R. *et al.* Pressure-Induced Split of the Density Wave Transitions in $La_3Ni_2O_{7-\delta}$. *Nat. Phys.* **21**, 430–436 (2025).

17. Luo, J. *et al.* Microscopic Evidence of Charge-and Spin-Density Waves in $La_3Ni_2O_{7-\delta}$ Revealed by ^{139}La-NQR. *Chin. Phys. Lett.* **42**, 067402 (2025).

18. Zhang, Y. *et al.* High-temperature superconductivity with zero resistance and strange-metal behaviour in $La_3Ni_2O_{7-\delta}$. *Nat. Phys.* **20**, 1269–1273 (2024).

19. Wang, G. *et al.* Pressure-Induced Superconductivity In Polycrystalline $La_3Ni_2O_{7-\delta}$. *Phys. Rev. X* **14**, 011040 (2024).

20. Liu, Z. *et al.* Electronic correlations and partial gap in the bilayer nickelate $La_3Ni_2O_7$. *Nat. Commun.* **15**, 7570 (2024).

21. Zhang, J. *et al.* Intertwined density waves in a metallic nickelate. *Nat. Commun.* **11**, 6003 (2020).

22. Xu, S. *et al.* Origin of the density wave instability in trilayer nickelate $La_4Ni_3O_{10}$ revealed by optical and ultrafast spectroscopy. *Phys. Rev. B* **111**, 075140 (2025).

23. Xu, S. *et al.* Collapse of density wave and emergence of superconductivity in pressurized-$La_4Ni_3O_{10}$ evidenced by ultrafast spectroscopy. *Nat. Commun.* **16**, 7039 (2025).

24. Khasanov, R. *et al.* Identical Suppression of Spin and Charge Density Wave Transitions in $La_4Ni_3O_{10}$ by Pressure. *arXiv:2503.04400* (2025).

25. Cao, Y. *et al.* Complex spin-density-wave ordering in $La_4Ni_3O_{10}$. *Phys. Rev. B* **112**, 174423 (2025).

26. Li, M. *et al.* Direct visualization of an incommensurate unidirectional charge density wave in $La_4Ni_3O_{10}$. *Phys. Rev. B* **112**, 045132 (2025).

27. Zhang, J. *et al.* High oxygen pressure floating zone growth and crystal structure of the metallic nickelates $R_4Ni_3O_{10}$ (R= La, Pr, and Nd). *Phys. Rev. Mater.* **4**, 083402 (2020).

28. Rout, D. *et al.* Structural and physical properties of trilayer nickelates $R_4Ni_3O_{10}$ (R= La, Pr, and Nd). *Phys. Rev. B* **102**, 195144 (2020).

29. Fukamachi, T., Kobayashi, Y., Miyashita, T. & Sato, M. ^{139}La NMR studies of layered perovskite systems $La_3Ni_2O_{7-\delta}$ and $La_4Ni_3O_{10}$. *J. Phys. Chem. Solids* **62**, 195–198 (2001).

30. Fukamachi, T., Oda, K., Kobayashi, Y., Miyashita, T. & Sato, M. Studies on Successive Electronic State Changes in Systems with NiO_2 Planes-^{139}La-NMR/NQR. *J. Phys. Soc. Jpn.* **70**, 2757–2764 (2001).

31. Kakoi, M. *et al.* Multiband Metallic Ground State in Multilayered Nickelates $La_3Ni_2O_7$ and $La_4Ni_3O_{10}$ Probed by ^{139}La-NMR at Ambient Pressure. *J. Phys. Soc. Jpn.* **93**, 053702 (2024).

32. Vinograd, I. *et al.* Locally commensurate charge-density wave with three-unit-cell periodicity in $YBa_2Cu_3O_y$. *Nat. Commun.* **12**, 3274 (2021).

33. Chou, F. C. *et al.* Magnetic phase diagram of lightly doped $La_{2-x}Sr_xCuO_4$ from ^{139}La nuclear quadrupole resonance. *Phys. Rev. Lett.* **71**, 2323 (1993).

34. Wu, T. *et al.* Magnetic-field-induced charge-stripe order in the high-temperature superconductor $YBa_2Cu_3O_y$. *Nature* **477**, 191–194 (2011).

35. Kawasaki, S. *et al.* Charge-density-wave order takes over antiferromagnetism in $Bi_2Sr_{2-x}La_xCuO_6$ superconductors. *Nat. Commun.* **8**, 1267 (2017).

36. Berezinskii, V. L. Destruction of long-range order in one-dimensional and two-dimensional systems possessing a continuous symmetry group. II. Quantum systems. *Sov Phys JETP* **34**, 610–616 (1972).

37. Kosterlitz, J. M. & Thouless, D. J. Long range order and metastability in two dimensional solids and superfluids.(Application of dislocation theory). *J. Phys. C Solid State Phys.* **5**, L124–L126 (1972).

38. Kosterlitz, J. M. & Thouless, D. J. Ordering, metastability and phase transitions in two-dimensional systems. *J. Phys. C Solid State Phys.* **6**, 1181–1203 (1973).

39. Janke, W. & Matsui, T. Crossover in the XY model from three to two dimensions. *Phys. Rev. B* **42**, 10673 (1990).

40. Singer, P. M., Arsenault, A., Imai, T. & Fujita, M. ^{139}La NMR investigation of the interplay between lattice, charge, and spin dynamics in the charge-ordered high-T_c cuprate $La_{1.875}Ba_{0.125}CuO_4$. *Phys. Rev. B* **101**, 174508 (2020).

41. Arsenault, A. *et al.* ^{139}La NMR investigation of the charge and spin order in a $La_{1.885}Sr_{0.115}CuO_4$ single crystal. *Phys. Rev. B* **97**, 064511 (2018).

42. Singer, P. M., Arsenault, A., Imai, T. & Fujita, M. ^{139}La NMR investigation of the interplay between lattice, charge, and spin dynamics in the charge-ordered high-T_c cuprate $La_{1.875}Ba_{0.125}CuO_4$. *Phys. Rev. B* **101**, 174508 (2020).

43. Julien, M.-H. *et al.* Glassy spin freezing and NMR wipeout effect in the high-T_c superconductor $La_{1.90}Sr_{0.10}CuO_4$: Critical discussion of the role of stripes. *Phys. Rev. B* **63**, 144508 (2001).

44. Baek, S.-H., Erb, A. & Büchner, B. Low-energy spin dynamics and critical hole concentrations in $La_{2-x}Sr_xCuO_4$ ($0.07 \leq x \leq 0.2$) revealed by ^{139}La and ^{63}Cu nuclear magnetic resonance. *Phys. Rev. B* **96**, 094519 (2017).

45. Baek, S.-H. *et al.* Magnetic field induced anisotropy of ^{139}La spin-lattice relaxation rates in stripe ordered $La_{1.87}Ba_{0.125}CuO_4$. *Phys. Rev. B* **92**, 155144 (2015).

46. Yang, Q.-G., Jiang, K.-Y., Wang, D., Lu, H.-Y. & Wang, Q.-H. Effective model and $s_{\pm}$-wave superconductivity in trilayer nickelate $La_4Ni_3O_{10}$. *Phys. Rev. B* **109**, L220506 (2024).

47. Qin, Q., Wang, J. & Yang, Y. Frustrated superconductivity and intrinsic reduction of T_c in trilayer nickelate. *Innov. Mater.* **2**, 100102–8 (2024).

48. Huang, J. & Zhou, T. Interlayer pairing-induced partially gapped Fermi surface in trilayer $La_4Ni_3O_{10}$ superconductors. *Phys. Rev. B* **110**, L060506 (2024).

49. Zhang, M. *et al.* $s^{\pm}$-wave superconductivity in pressurized $La_4Ni_3O_{10}$. *Phys. Rev. B* **110**, L180501 (2024).

50. Lu, C., Pan, Z., Yang, F. & Wu, C. Superconductivity in $La_4Ni_3O_{10}$ under pressure. *Phys. Rev. B* **111**, 134515 (2025).

51. Wu, T. *et al.* Incipient charge order observed by NMR in the normal state of $YBa_2Cu_3O_y$. *Nat. Commun.* **6**, 6438 (2015).

52. Haase, J., Slichter, C. P., Stern, R., Milling, C. T. & Hinks, D. G. Spatial Modulation of the NMR Properties of the Cuprates. *Phys. C Supercond.* **341**, 1727–1730 (2000).

53. LaBollita, H., Kapeghian, J., Norman, M. R. & Botana, A. S. Electronic structure and magnetic tendencies of trilayer $La_4Ni_3O_{10}$ under pressure: Structural transition, molecular orbitals, and layer differentiation. *Phys. Rev. B* **109**, 195151 (2024).

54. Zhang, M. *et al.* Spin-density wave and superconductivity in $La_4Ni_3O_{10}$ under ambient pressure. *Phys. Rev. B* **111**, 144502 (2025).

55. Li, H. *et al.* Fermiology and electron dynamics of trilayer nickelate $La_4Ni_3O_{10}$. *Nat. Commun.* **8**, 704 (2017).

56. Li, Y. *et al.* Distinct ultrafast dynamics of bilayer and trilayer nickelate superconductors regarding the density-wave-like transitions. *Sci. Bull.* **70**, 180–186 (2025).

57. Oliviero, V. *et al.* Charge order near the antiferromagnetic quantum critical point in the trilayer high T_c cuprate $HgBa_2Ca_2Cu_3O_{8+\delta}$. *Npj Quantum Mater.* **9**, 75 (2024).

58. Leonov, I. V. Electronic structure and magnetic correlations in the trilayer nickelate superconductor $La_4Ni_3O_{10}$ under pressure. *Phys. Rev. B* **109**, 235123 (2024).

59. Wang, J.-X., Ouyang, Z., He, R.-Q. & Lu, Z.-Y. Non-Fermi liquid and Hund correlation in $La_4Ni_3O_{10}$ under high pressure. *Phys. Rev. B* **109**, 165140 (2024).

60. Huo, Z., Zhang, P., Zhang, Z., Duan, D. & Cui, T. Electronic Correlations and Hund's Rule Coupling in Trilayer Nickelate $La_4Ni_3O_{10}$. *Sci. China Phys. Mech. Astron.* **68**, (2025).

61. Zhang, Y., Lin, L.-F., Moreo, A., Maier, T. A. & Dagotto, E. Prediction of $s_{\pm}$-wave superconductivity enhanced by electronic doping in trilayer nickelates $La_4Ni_3O_{10}$ under pressure. *Phys. Rev. Lett.* **133**, 136001 (2024).

62. Xie, T. *et al.* Strong interlayer magnetic exchange coupling in $La_3Ni_2O_{7-\delta}$ revealed by inelastic neutron scattering. *Sci. Bull.* **69**, 3221–3227 (2024).

Acknowledgements

We are thankful for the valuable discussions with Kun Jiang and Xianhui Chen.

Funding

Y.W., D.Z., Y.B.Z. and T.W. disclose support for the research of this work from the National Key R&D Program of the MOST of China [Grant No. 2022YFA1602601] and the National Natural Science Foundation of China [Grant No. 12325403, 12034004, 12161160316]. J.J.Y., M.Z.S. and T.W. disclose support from the National Natural Science Foundation of China [Grant No. 12488201], the CAS Project for Young Scientists in Basic Research [Grant No. YBR-048], and the Innovation Program for Quantum Science and Technology [Grant No. 2021ZD0302800]. J.J.Y. and M.Z.S. disclose support from the National Natural Science Foundation of China [Grant No. 12494592]. Y.W., D.Z., Y.B.Z., M.Z.S., J.J.Y. and T.W. disclose support from the CAS Superconducting Research Project [Grant No. SCZX-0101] and the Innovation Program for Quantum Science and Technology [Grant No. 2021ZD0302800]. J.J.Y. and T.W. disclose support from the Chinese Academy of Sciences [Grant No. JZHKYPT-2021-08]. E.K.Z., L.X.C. and J.Z. disclose support from the National Natural Science Foundation of China [Grant No. 12234006], the National Key R&D Program of China [Grant No. 2022YFA1403202], and the Innovation Program for Quantum Science and Technology [Grant No. 2024ZD0300103].

Author contributions

T.W. conceived the research project and coordinated the experiments. E.K.Z., L.X.C. and J.Z. grew the single crystals. Y.W. performed the structural characterization at ambient pressure with the help of M.Z.S. and J.J.Y.. Y.W., D.Z. and Y.B.Z. performed the NMR measurements. Y.W., D.Z. and T.W. analysed the data. Y.W., D.Z. and T.W. wrote the paper with input from all the authors.

Competing interests

The authors declare no competing interests.

Figures

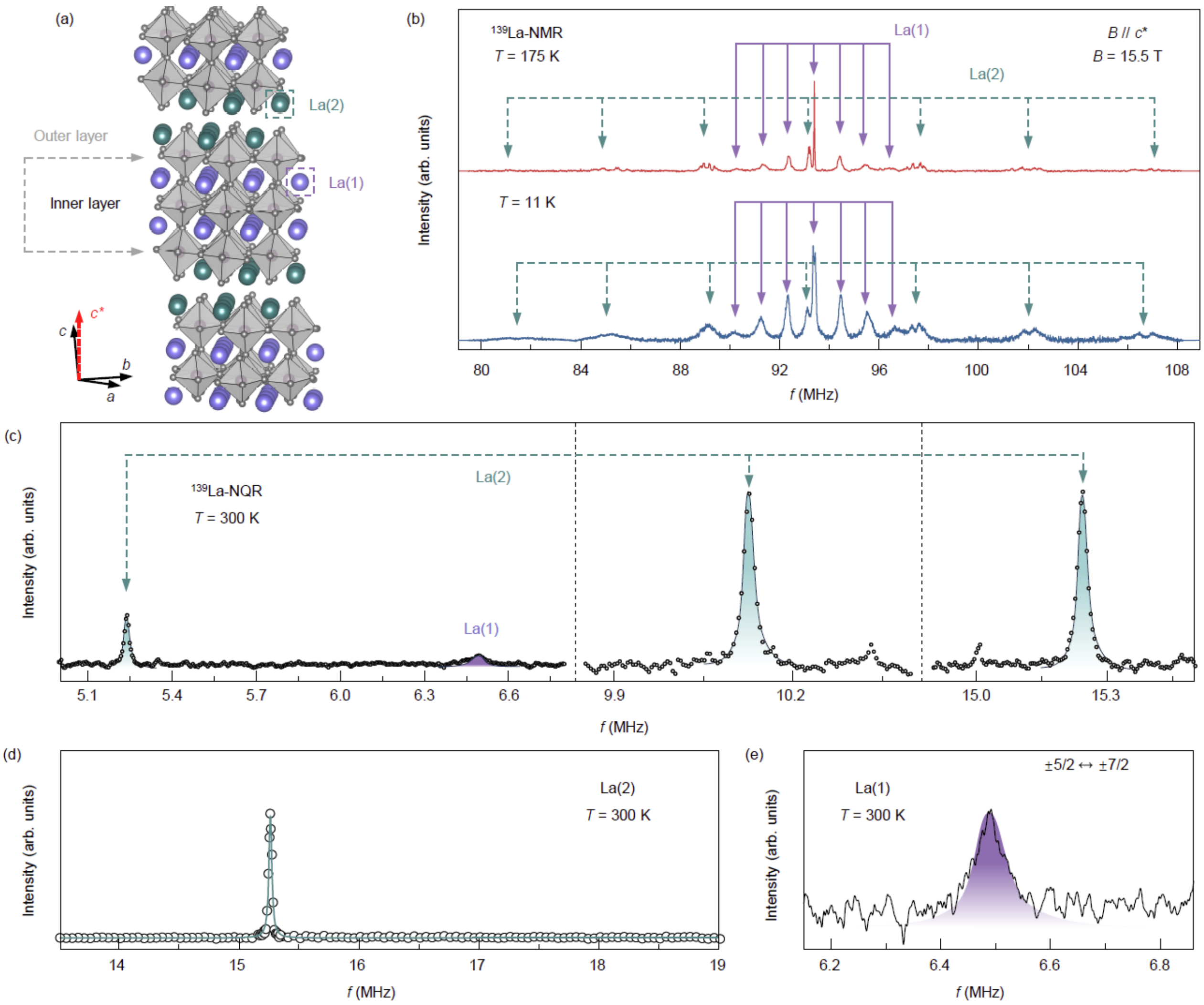

Fig. 1 | Characterization of NMR spectra and ^{139}La site assignments. (a) Schematic of the $La_4Ni_3O_{10}$ crystal structure. Owing to the monoclinic structure symmetry, the *c*-axis is not perpendicular to the *ab*-plane. For convenience, we can define the *c**-axis as the direction normal to the *ab*-plane. The La sites located within the inner Ni-O block are designated as La(1) (marked by a purple dashed line), whereas the La sites outside the trilayer Ni-O plane are designated as La(2) (marked by a green dashed line). (b) Full ^{139}La NMR spectra above and below the DW transition. The purple solid lines and green dashed lines mark the transition lines for the La(1) and La(2) sites, respectively. (c) ^{139}La-NQR spectra at 300 K. The solid lines represent Lorentz fits. Three resonance lines, marked in green, are observed for La(2) sites. One resonance line corresponding to the $\pm 5/2 \leftrightarrow \pm 7/2$ transition is observed for the La(1) site. (d) Broad frequency-sweep NQR spectrum spanning 13.5 to 19 MHz at T = 300 K. The solid line represents Lorentz fit. (e) La(1) NQR spectrum corresponding to the $\pm 5/2 \leftrightarrow \pm 7/2$ transition at T = 300 K.

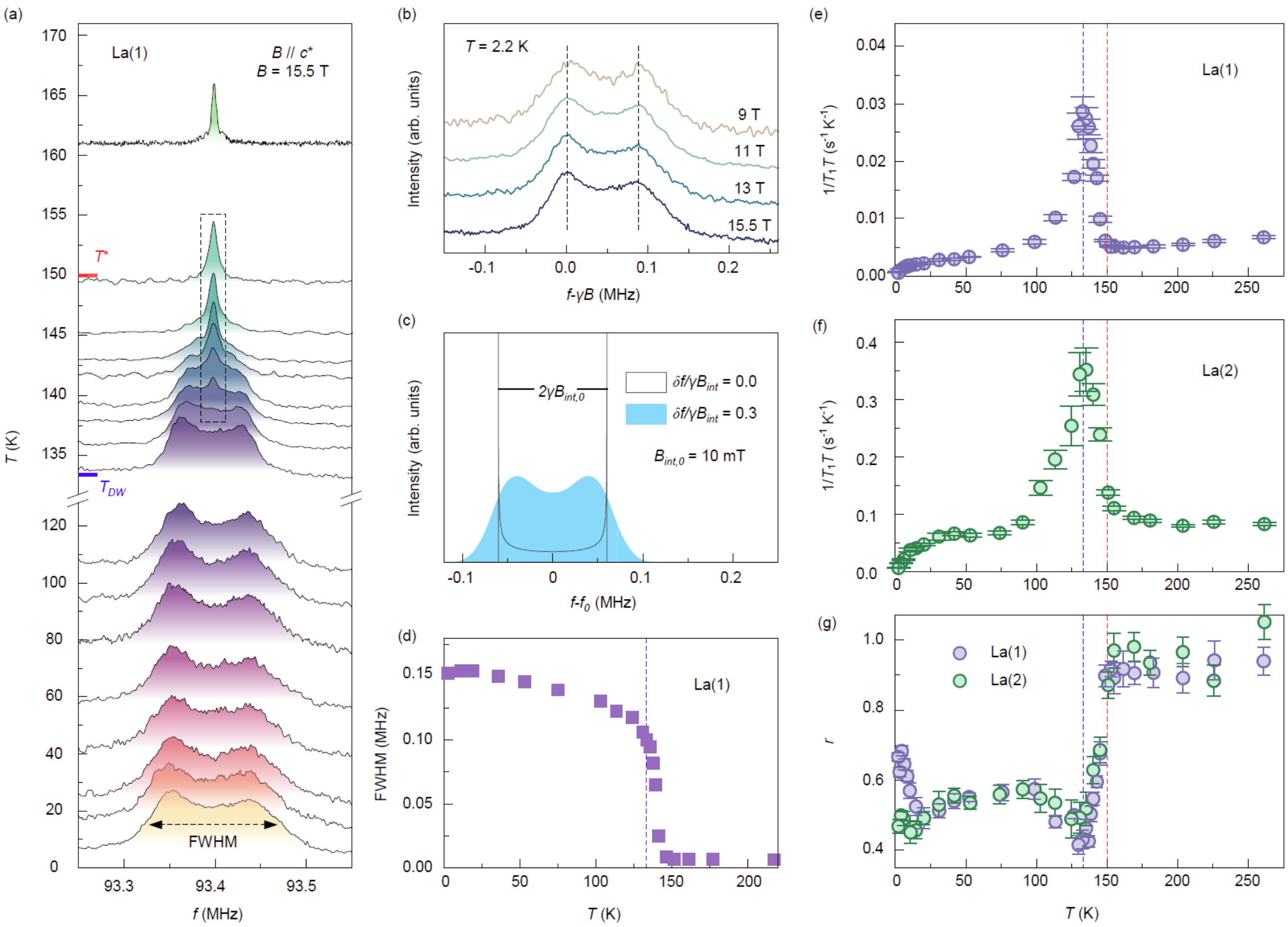

Fig. 2 | Evidence for a spin–density–wave transition. (a) Temperature-dependent central transition lines for the La(1) site. The dashed rectangle highlights the paramagnetic-state component as a visual guide. The double-headed arrow indicates the full width at half maximum (FWHM) referenced in (d). (b) Magnetic-field-dependent central transition lines at the La(1) site, measured from 15.5 T to 9 T. The dashed lines mark the positions of the peaks. (c) Simulated results for an incommensurate spin modulation. The oscillatory internal magnetic field ($B_{int}(x)$) has a maximum field strength ($B_{int,0}$) and a phase (φ_s), expressed as $B_{int}(x) = B_{int,0}\cdot\cos(q_s\cdot x + \varphi_s)$. The black line represents the characteristic resonance frequency distribution histogram, featuring two singularities at the extremal values of the internal field and a continuum of intensity in between. Convolution with a Gaussian function (width $\delta f/\gamma B_{int} = 0.3$) yields a double-peak-like lineshape filled in color. (d) Temperature-dependent FWHM of the central transition line at the La(1) site, extracted from the data in (a). (e)-(f) Temperature-dependent spin-lattice relaxation rate divided by temperature ($1/T_1T$) at the (e) La(1) and (f) La(2) sites. (g) Temperature-dependent stretched exponent r at the La(1) and La(2) sites. The red and blue dashed lines in panels (d)-(g) represent the temperatures corresponding to $T^* \approx 150$ K and $T_{DW} \approx 133$ K, respectively.

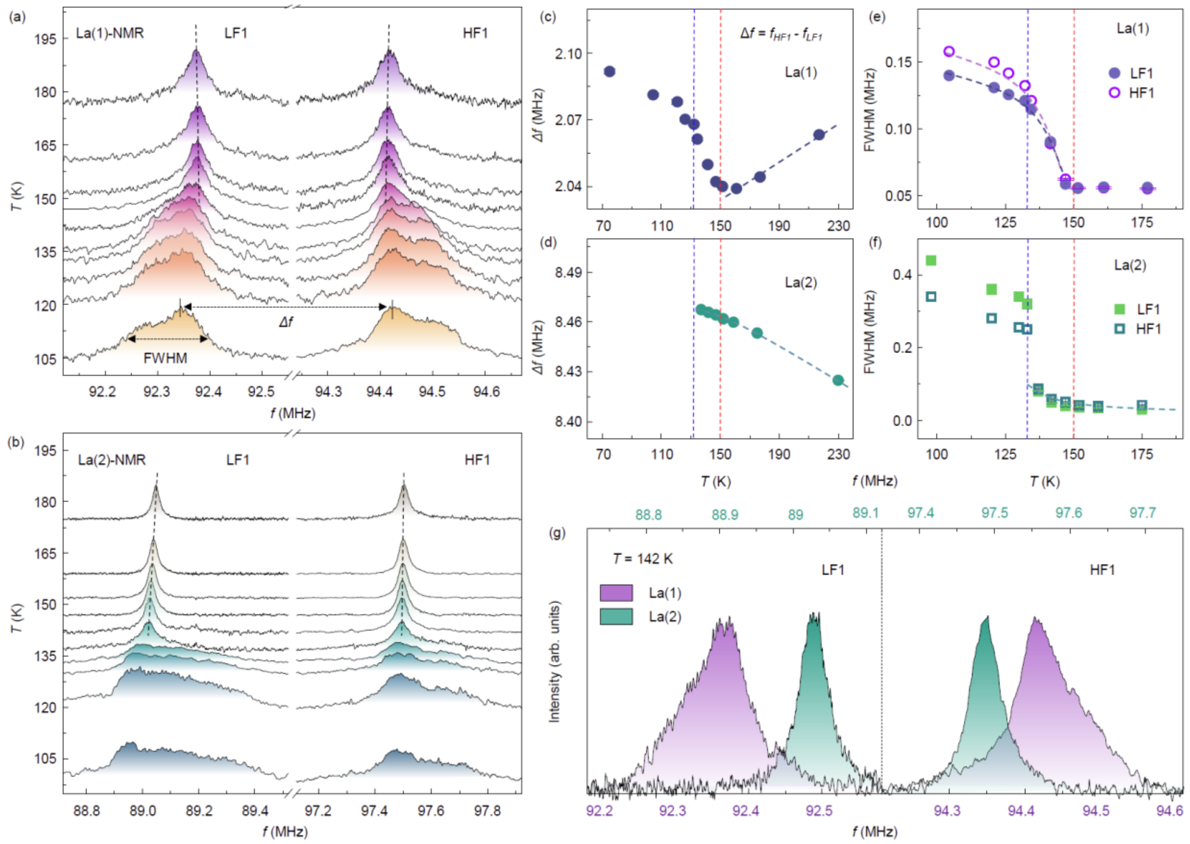

Fig. 3 | Evidence for a charge anomaly from NMR satellites. (a)-(b) First low-frequency (LF1) and high-frequency (HF1) satellites as a function of temperature at the (a) La(1) and (b) La(2) sites. The dashed lines trace the temperature evolution of resonance peaks. (c)-(d) Temperature dependence of the frequency difference (Δf) between the HF1 and LF1 satellites at the (c) La(1) and (d) La(2) sites. Here, Δf is defined as $\Delta f = f_{\mathrm{HF1}} - f_{\mathrm{LF1}}$, where f_{HF1} and f_{LF1} represent the resonance frequencies of the HF1 and LF1, respectively. (e)-(f) Temperature dependence of the FWHM for the HF1 and LF1 satellites at (e) La(1) and (f) La(2) sites. (g) LF1 and HF1 for the La(1) and La(2) sites at $T = 142$ K. The lineshape for the La(1) site exhibits a pronounced asymmetry, in stark contrast to that for the La(2) site. The red and blue dashed lines in panels (c)-(f) represent the temperatures corresponding to $T^* \approx 150$ K and $T_{DW} \approx 133$ K, respectively.

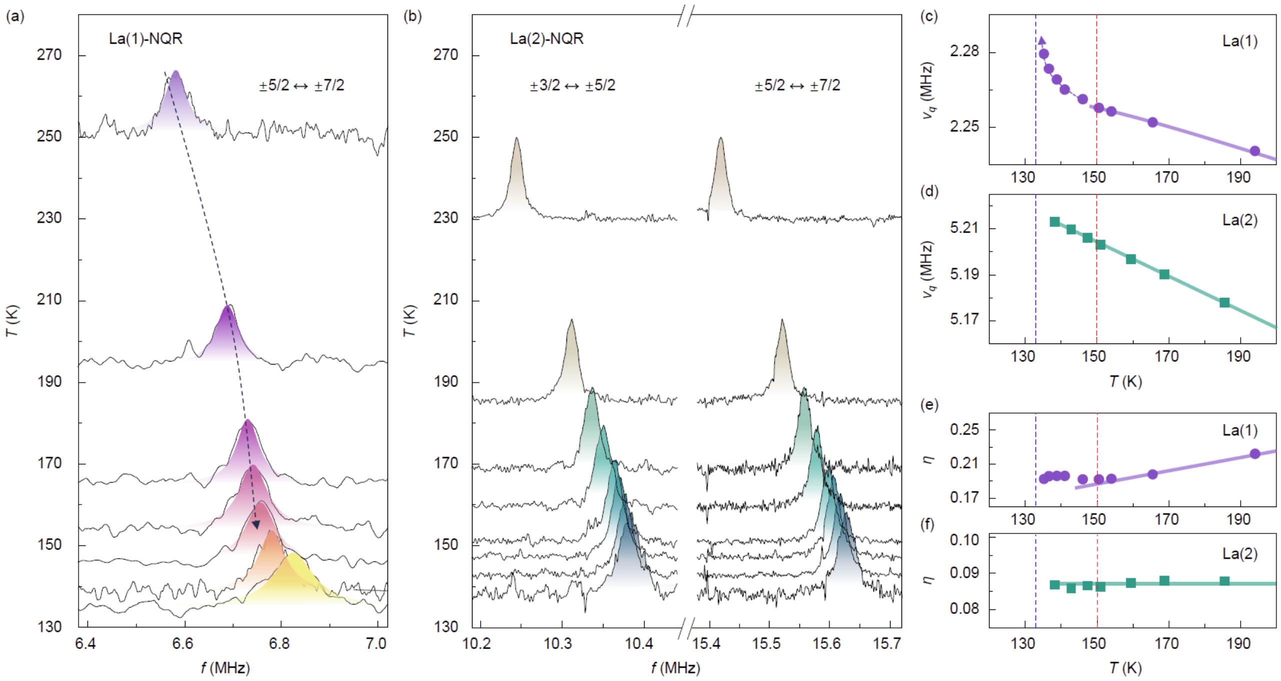

Fig. 4 | Evidence for a short-range charge order in the inner layer from NQR spectra. (a) Temperature dependence of the La(1) NQR spectra corresponding to ±5/2 ↔ ±7/2 ($3\nu_q$) transition. The dotted arrow traces the temperature evolution of the resonance peaks. (b) Temperature dependence of the NQR spectra at the La(2) site associated with ±3/2 ↔ ±5/2 ($2\nu_q$) and ±5/2 ↔ ±7/2 ($3\nu_q$) transitions. (c)-(d) Temperature dependence of the quadrupole frequency ν_q for the La(1) and La(2) sites, respectively. (e)-(f) Temperature dependence of the asymmetry parameter η for the La(1) and La(2) sites. The EFG parameters for the La(1) sites were determined by analysing the frequencies of satellites in Fig. 3(c) and the NQR-$3\nu_q$ transitions in Fig. 4(a), assuming fixed values for θ and φ (Supplementary Note 8). For the La(2) site, the EFG parameters were extracted from the resonance frequencies of the $2\nu_q$ and $3\nu_q$ transitions in the NQR spectra shown in Fig. 4(b). The red and blue dashed lines in panels (c)–(f) represent the temperatures corresponding to $T^* \approx 150$ K and $T_{DW} \approx 133$ K, respectively.

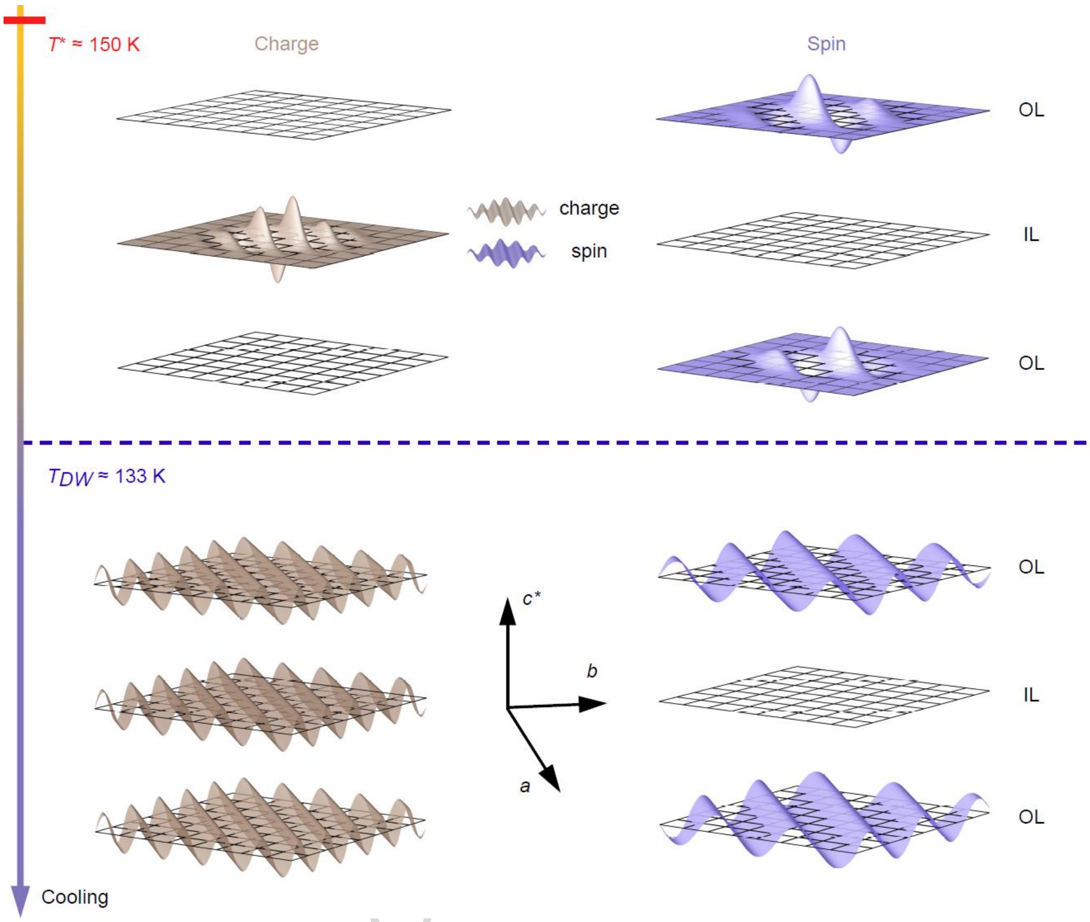

Fig. 5 | Schematic of the temperature evolution of DW order in the Ni lattice model. The representation of Ni atoms occupying each lattice site is omitted for clarity. The cooling process is indicated by the downward arrow, with characteristic temperatures $T^* \approx 150$ K and $T_{DW} \approx 133$ K marked by horizontal lines. The left column illustrates the evolution of the charge degrees of freedom, while the right column depicts the evolution of the spin degrees of freedom. The trilayer structure is labelled as outer (OL) and inner (IL) layers. The charge and spin density modulations are represented by the brown and purple shapes, respectively. For charge degrees of freedom, a short-range charge order initially emerges in the inner Ni-O layer at $T \approx 150$ K. Upon further cooling, a long-range CDW order develops across the trilayer Ni-O plane at $T_{\mathrm{DW}} \approx 133$ K. Meanwhile, the spin degrees of freedom undergo a similar evolution from short-range correlations to long-range order, although our ^{139}La-NMR measurements cannot fully resolve the layer-dependent features of the SDW. Previous neutron scattering data indicated an absence of magnetic order in the inner layer [21], which is adopted in the present schematic.

Editorial Summary:

The authors reveal a two-stage formation of density-wave order in nickelate La4Ni3O10 at ambient pressure. First, a short-range charge order develops in the inner Ni-O layer, accompanied by a dramatic enhancement of spin fluctuations, followed by fully-developed charge and spin orders at lower temperature.

Peer review information: *Nature Communications* thanks Shunsaku Kitagawa, and the other, anonymous, reviewer(s) for their contribution to the peer review of this work. A peer review file is available.